Chemical Engineering Journal Advances 14 (2023) 100448

Contents lists available at ScienceDirect

Chemical Engineering Journal Advances

journal homepage: www.sciencedirect.com/journal/chemical-engineering-journal-advances

Computational study of three-dimensional Lagrangian transport and mixing in a stirred tank reactor

Christian Weiland [*,1,a], Eike Steuwe [a], Jürgen Fitschen [a], Marko Hoffmann [a], Michael Schlüter [a], Kathrin Padberg-Gehle [c], Alexandra von Kameke [b]

[a] *Institute of Multiphase Flows, Hamburg University of Technology, Eißendorfer Straße 38, Hamburg 21073, Germany*
[b] *Department of Mechanical Engineering and Production Management, Hamburg University of Applied Sciences, Berliner Tor 21, Hamburg 20099, Germany*
[c] *Institute of Mathematics and its Didactics, Leuphana University Lüneburg, Universitätsallee 1, Lüneburg 21335, Germany*

ARTICLE INFO

Keywords:
Lagrangian coherent structures
Mixing
Finite time lyapunov exponent
Stirred tank reactor
Compartments
Network methods

ABSTRACT

The detection of compartments and dead zones as well as the estimation of the mixing efficiency in stirred tanks are of vital interest for a variety of biochemical and chemical processes. Here, numerically derived time-dependent 3D fluid velocity fields of a stirred tank reactor are computed using the Lattice Boltzmann Method. Mixing in the stirred tank reactor is analysed by means of Lagrangian Coherent Structures which allow to unravel the mixing states of complex flows. This Lagrangian analysis is achieved by computing Finite Time Lyapunov Exponents and applying recent trajectory-based network methods on the three-dimensional flow. The results reveal a zone of low interaction in the upper region of the stirred tank reactor and five additional transient compartments. The trajectory-based network analysis detects low cross-mixing of fluid parcels between different compartments but a very high mixing of fluid parcels inside of each compartment. This high interaction is also found in an analysis of the Finite Time Lyapunov Mixing Intensity. Time-averaging of the fluid velocity field prior to the Lagrangian analysis is considered to extract the most influential Lagrangian Coherent Structures.

1. Introduction

In the chemical and biochemical industry, mixing plays a key role for the efficiency of many processes [1]. A fast and homogeneous, or at least a defined and adjustable mixing efficiency is crucial for many chemical reactions, especially if several parallel or consecutive reactions are involved [2]. Additionally, a high mixing quality is crucial in the course of strongly exothermic reactions to prevent the hazard of dead zones and temperature hot spots, which can lead to a thermal runaway [3]. In biochemical processes often a sufficient supply and discharge of oxygen, carbon dioxide and substrates is essential for the growth and activity of biological cells [4].

In the past and up to this point stirred tank reactors (STR) have been the workhorses in the (bio)chemical industry [5] and are still subject of recent research [6–15]. In the course of processes carried out in STRs, the fluid flow has a dominant influence on the mixing efficiency and on the occurrence of compartments. The latter already have been studied intensively [4,16–19], identifying them as time-evolving regions with a major impact on the whole process. To examine these time dependent and therefore transient compartments and their occurrence in the temporally evolving fluid flow, the consideration of *Lagrangian Coherent Structures* (LCS), which were first mentioned by Haller and Yuan [20], seems a promising route. An LCS is to be thought of as a simply coherent material line (in 2D) or surface (in 3D) $\mathscr{M}(t)$ [20–22], which has a strong influence on the flow nearby and shapes the mixing. Two different kinds of LCSs are depicted in Fig. 1. An attracting LCS (aLCS) maximally attracts fluid elements close to it, while a repelling LCS (rLCS) maximally repels them. This attraction and repulsion is strongly related to the aforementioned formation of transient compartments since these LCSs usually enclose areas of low mixing. Additionally, the hyperbolic points, where both kinds of LCSs cross each other, have a direct influence on the mixing efficiency. The impact of LCSs on several complex flows has experienced high attention from several groups such as Haller et al.

Abbreviations: BFTLE, Backward Finite Time Lyapunov Exponent; CGST, Right Cauchy-Green-Strain-Tensor; FFTLE, Forward Finite Time Lyapunov Exponent; FTLE, Finite Time Lyapunov Exponent; FTLMI, Finite Time Lyapunov Mixing Intensity; LBM, Lattice Boltzmann Method; LCS, Lagrangian Coherent Structure; LES, Large Eddy Simulation; SEBA, Sparse Eigenbasis Approximation; STR, Stirred Tank Reactor.

[*] Corresponding author.
E-mail address: christian.weiland@tuhh.de (C. Weiland).

[1] orcid: 0000-0003-3321-987X

https://doi.org/10.1016/j.ceja.2023.100448
Received 7 December 2022; Received in revised form 10 January 2023; Accepted 11 January 2023

Nomenclature

Arabic symbols

Δt	integration time
$\mathscr{M}(t)$	material line/surface at time t
$\mathscr{O}$	Landau symbol
$\mathscr{T}$	time interval
$\boldsymbol{A}$	adjacency matrix
$\boldsymbol{C}$	right cauchy-green-strain-tensor
$\boldsymbol{D}$	degree matrix
$\boldsymbol{F}$	flow map
$\boldsymbol{I}$	identity matrix
$\boldsymbol{J}_{\boldsymbol{\Phi}}$	jacobian of the function $\boldsymbol{\Phi}$
$\boldsymbol{L}$	non-normalised Laplacian
$\boldsymbol{Q}$	orthogonal matrix from the polar decomposition
$\boldsymbol{R}$	symmetric positive definite matrix from the polar decomposition
$\boldsymbol{U}$	basis of the vector space $\mathscr{U}$
$\boldsymbol{u}$	basis vector of the vector space $\mathscr{U}$
$\boldsymbol{V}$	basis of the vector space $\mathscr{V}$
$\boldsymbol{v}$	basis vector of the vector space $\mathscr{V}$
$\boldsymbol{W}$	weight matrix
$\boldsymbol{w}$	velocity
$\boldsymbol{w}_{a,b,c,d}$	approximated velocity at position $\boldsymbol{x}_{a,b,c}$ at time t_d
$\boldsymbol{x}$	position
C^n	space of functions which are n times steadily differentiable
f	particle distribution function
K	collision parameter
n	stirrer frequency
$S_{\max}$	cluster indicator
t_{R}	relaxation time
V	volume

Greek symbols

η	dynamic viscosity
Λ^+	forward finite time Lyapunov exponent
Λ^-	backward finite time Lyapunov exponent
λ_i	eigenvalue
Ω	geometric space
ρ	density
θ	angle
$\widetilde{\Lambda}$	finite time Lyapunov mixing intensity
ϑ	temperature
$\boldsymbol{\gamma}$	distance between particles
$\boldsymbol{\xi}_i$	eigenvector corresponding to the eigenvalue λ_i of the matrix $\boldsymbol{R}$
$\boldsymbol{\zeta}$	microscopic velocity of particles concerning the Lattice Boltzmann simulation

[20–24], Shadden et al. [25–28], Balasuriya et al. [29–31], Brunton et al. [32–34] and von Kameke et al. [35,36]. Very recently, LCSs were analysed in a stirred tank by Li et al. [37], who proposed the usage of time-averaged experimental data for the identification of LCSs in a stirred tank reactor with one pitched blade turbine.

Originally, the study of LCSs requires knowledge of the smooth flow map of fluid elements from which Finite Time Lyapunov Exponents (FTLE) are computed. These measure the growth of small perturbations, and thus serve as a stretching indicator. While the extraction of material lines in 2D flows has been automated by Onu et al. [24] in MATLAB's LCS-Tool, the identification of evolving material surfaces in 3D flows remains challenging. Several articles [38–40] have been published in this field in which different approaches were utilised and the advantages and disadvantages of Lagrangian methods over Eulerian methods were discussed. The reviews [41,42] discuss the different, frequently used Lagrangian approaches. Among them are probabilistic methods [43], which provide a complementary view compared to the flow map approaches in identifying and extracting time evolving fluid volumes that minimally mix with the surrounding fluid. Recently, data-based approaches have been proposed [44–47] that can directly deal with Lagrangian tracer trajectories in order to study and quantify coherent compartments. Trajectory-based network methods that define coherent sets via clusters in a flow network have been proven very efficient [45, 48–50].

The aim of the present work is to identify LCSs and coherent fluid volumes in a stirred tank reactor by means of the FTLE and trajectory-based network methods to achieve greater knowledge about optimal feed positions and the overall mixing process in an STR. The observed vessel is a laboratory scale STR with two Rushton turbines and three baffles that has been studied in previous works [10,51,52]. The fluid velocity field in the STR is calculated by the application of the Lattice Boltzmann Method (LBM) by using the programme M-Star CFD (M-Star Simulations, LCC.).

The paper is organised as follows: In Section 2, the stirred tank reactor setup is described, the FTLE framework and the trajectory-based network methods are introduced, and details on the Computational Fluid Dynamics (CFD) simulation of the flow in the STR and the 3D FTLE implementation are presented. In Section 3, the results of the Lagrangian analysis are presented and discussed. First, the FTLE fields in forward and backward times and for different integration times and two different stirrer frequencies are considered. Afterwards, these results are compared with the coherent, transient compartments identified from the

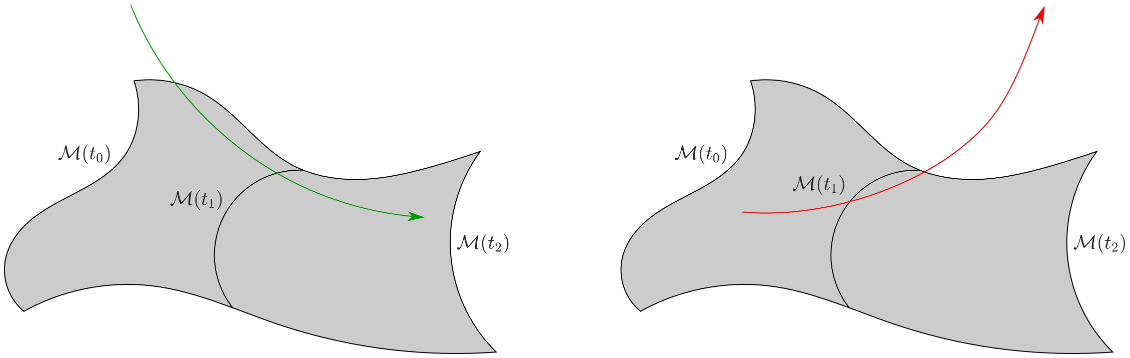

Fig. 1. Attracting LCS (left) and repelling LCS (right) according to Haller [38]. The coloured arrow indicates the trajectory of a fluid element nearby the respective LCS.

trajectory-based network approach. Finally, it is demonstrated that the Lagrangian results obtained via the combination of FTLE analysis and trajectory-based network methods allow to obtain very detailed insights on transport, mixing and zones of low interaction in the vessel. The mixing structures differ largely from those obtained from time-averaged velocity fields. A discussion regarding the implications of these findings and a comparison with experimental data [10] is presented in Section 4.

2. Material and methods

For an overview over the topics of this work, the following sections will introduce the used reactor setup, the numerical framework and the relevant physical and mathematical analysis methods.

2.1. Stirred tank reactor setup

The numerical model of the STR has previously been introduced and experimentally validated by Kuschel et al., Hofmann et al. and Fitschen [10,51,52]. It has a working volume of $V_{\mathrm{STR}} = 2.8\,\mathrm{L}$. The reactor has a korbbogen head bottom, three baffles with an angular offset of $\theta = 2\pi/3$ and two Rushton turbines. The relevant dimensions can be taken from Fig. 2. The numerical properties of the fluid are those of water at $\vartheta = 20\,^{\circ}\mathrm{C}$ ($\rho_{\mathrm{F}} = 998.2\,\mathrm{kg\,m^{-3}}$, $\eta = 1.0016\,\mathrm{mPa\,s}$). The flow in these systems is known to be turbulent for Reynolds numbers $Re := \frac{n d_{\mathrm{R}}^2 \rho_{\mathrm{F}}}{\eta} \geq 10^4$, where n is the stirrer frequency [53]. For the observed reactor the critical stirrer frequency is $n_{\mathrm{crit}} \approx 465\,\mathrm{rpm}$.

2.2. Theoretical background

The first part of this section deals with the derivation and definition of the FTLE and the examination of its connection to the deformation of fluid elements. The second part gives insight into the trajectory-based network methods. In the third part, a short description of the numerical method to compute the fluid velocity field follows. The final part of this chapter explains the implemented algorithms and the procedure that integrates the methods mentioned above for further analysis.

2.2.1. Deformation of fluid elements and the Finite Time Lyapunov Exponent

Let $\boldsymbol{w} \in C^2$ denote the velocity field of a fluid inside a given geometry $\Omega \subseteq \mathbb{R}^3$ for a given time interval $\mathscr{T} \subseteq \mathbb{R}$. It is assumed that fluid elements or non-inertial particles will follow the flow perfectly. The trajectory $\boldsymbol{x}(t) \in \Omega$, $t \in \mathscr{T}$ of a tracer is obtained via the solution of the initial value problem

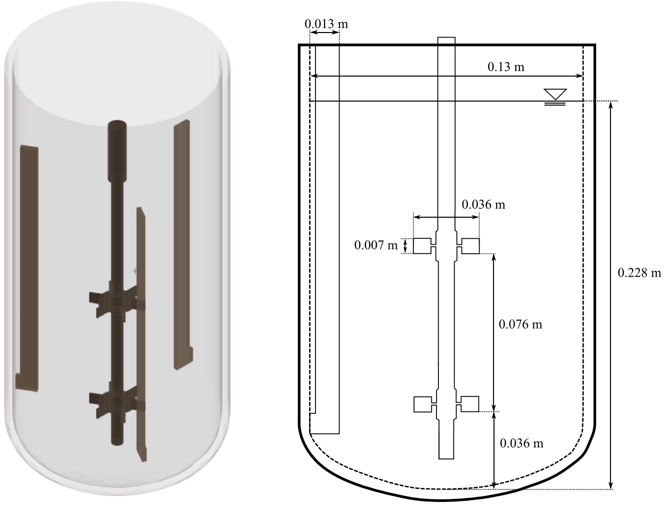

Fig. 2. Geometric setup and dimensions of the STR.

$$\dot{\boldsymbol{x}}(t) = \boldsymbol{w}(\boldsymbol{x}(t), t), \quad \boldsymbol{x}(t_0) = \boldsymbol{x}_0 \tag{1}$$

and thus

$$\boldsymbol{x}(t) = \boldsymbol{x}_0 + \int_{t_0}^{t} \boldsymbol{w}(\boldsymbol{x}(\tau), \tau) d\tau, \ t \in \mathscr{T} \tag{2}$$

Fixing the initial time t_0 and final time t_{F}, the flow map $\boldsymbol{F}_{t_0}^{t_{\mathrm{F}}} : \Omega \rightarrow \Omega$ can be defined as the solution operator of the underlying ordinary differential equation $\dot{\boldsymbol{x}}(t) = \boldsymbol{w}(\boldsymbol{x}(t), t)$ on $[t_0, t_{\mathrm{F}}] \subset \mathscr{T}$. Hence, $\boldsymbol{F}_{t_0}^{t_{\mathrm{F}}}$ maps the initial tracer position $\boldsymbol{x}_0$ to its final position $\boldsymbol{F}_{t_0}^{t_{\mathrm{F}}}(\boldsymbol{x}_0) = \boldsymbol{x}(t_{\mathrm{F}})$ at time t_{F}. For means of clarity the indices and arguments of the flow map are omitted in the following. If not stated differently, $\boldsymbol{F}$ will always refer to $\boldsymbol{F}_{t_0}^{t_{\mathrm{F}}}(\boldsymbol{x}_0)$.

For two particles i and j, their distance vector at time $t \in \mathscr{T}$

$$\boldsymbol{\gamma}(t) := \boldsymbol{x}_j(t) - \boldsymbol{x}_i(t) \tag{3}$$

is considered and consequently, the position of particle j can be rewritten as a Taylor series

$$\begin{aligned} \boldsymbol{x}_j(t) &= \boldsymbol{x}_{i,0} + \boldsymbol{\gamma}_0 + \int_{t_0}^{t} \boldsymbol{w}(\boldsymbol{x}_i(\tau) + \boldsymbol{\gamma}(\tau), \tau) d\tau \\ &= \boldsymbol{x}_{i,0} + \boldsymbol{\gamma}_0 + \int_{t_0}^{t} \boldsymbol{w}(\boldsymbol{x}_i(\tau), \tau) + \boldsymbol{J}_{\boldsymbol{w}} \cdot \boldsymbol{\gamma}(\tau) + \mathscr{O}\left(\| \boldsymbol{\gamma}(\tau) \|_2^2\right) d\tau, \end{aligned} \tag{4}$$

where $\boldsymbol{J}_{\boldsymbol{w}}$ denotes the Jacobian of the velocity field $\boldsymbol{w}$ at the position $\boldsymbol{x}_i$. The magnitude of the distance $\| \boldsymbol{\gamma}(t) \|_2$ is assumed to be small, hence neglecting higher order terms in Eq. (4), inserting Eqs. (2 and 4) into Eq. (3) and differentiating the result with respect to time yields the variational equation [54]

$$\dot{\boldsymbol{\gamma}}(t) = \boldsymbol{J}_{\boldsymbol{w}} \cdot \boldsymbol{\gamma}(t), \ \text{with} \ \boldsymbol{\gamma}(t_0) = \boldsymbol{\gamma}_0, \tag{5}$$

which describes the evolution of the distance vector $\boldsymbol{\gamma}(t)$ between close particles starting at positions $\boldsymbol{x}_{i,0}$ and $\boldsymbol{x}_{j,0}$, respectively. The evolution of the distance $\boldsymbol{\gamma}(t)$ is depicted schematically in Fig. 3. This equation holds true while the magnitude of the distance $\| \boldsymbol{\gamma}(t) \|_2$ is sufficiently small. The solution of Eq. (5) and evaluation at time t_{F} is given by

$$\boldsymbol{\gamma}(t_{\mathrm{F}}) = \boldsymbol{J}_{\boldsymbol{F}} \cdot \boldsymbol{\gamma}_0, \tag{6}$$

which can be checked easily by inserting the solution into the differential equation Eq. (5). Hereby $\boldsymbol{J}_{\boldsymbol{F}}$ denotes the Jacobian of the flow map. In other words: An initial deviation $\boldsymbol{\gamma}_0$ between particles around position $\boldsymbol{x}_0$ at time t_0 will be transformed linearly by the Jacobian of the flow map to another deviation $\boldsymbol{\gamma}(t_{\mathrm{F}})$ between the same particles at time t_{F}. For means of clarity, the argument t_{F} in $\boldsymbol{\gamma}(t_{\mathrm{F}})$ will be omitted.

The identification of compartments and regions of strong mixing behaviour is related to the identification of regions where high deformations according to Eq. (6) arise [55,56]. Each matrix $\boldsymbol{A} \in \mathbb{R}^{n \times n}$ can be decomposed into an orthogonal matrix $\boldsymbol{Q} \in \mathbb{R}^{n \times n}$ and a symmetric positive (semi) definite Matrix $\boldsymbol{R} \in \mathbb{R}^{n \times n}$ [57]. Since this work deals with problems where continuity holds, the matrix $\boldsymbol{R}$ has a determinant of $\det \boldsymbol{R} = 1$ [58], hence it is definite. This polar decomposition can be used on the Jacobian of the flow map

$$\boldsymbol{J}_{\boldsymbol{F}} = \boldsymbol{Q}\boldsymbol{R} \Rightarrow \boldsymbol{\gamma} = \boldsymbol{Q}\boldsymbol{R} \cdot \boldsymbol{\gamma}_0. \tag{7}$$

The matrix $\boldsymbol{R}$ is responsible for deformation due to stretching, shrinking and shear, thus increasing or decreasing the magnitude of an initial deviation $\boldsymbol{\gamma}_0$. The matrix $\boldsymbol{Q}$ on the other hand is responsible only for pure rotation. To be able to state which degree of deformation occurs, the inner product

$$\boldsymbol{\gamma}^T \boldsymbol{\gamma} = \boldsymbol{\gamma}_0^T \cdot (\boldsymbol{J}_{\boldsymbol{F}})^T \boldsymbol{J}_{\boldsymbol{F}} \cdot \boldsymbol{\gamma}_0 = \boldsymbol{\gamma}_0^T \boldsymbol{R}^T \underbrace{\boldsymbol{Q}^T \boldsymbol{Q}}_{\equiv \boldsymbol{I}} \boldsymbol{R} \boldsymbol{\gamma}_0 = \boldsymbol{\gamma}_0^T \underbrace{\boldsymbol{R}^T \boldsymbol{R}}_{=:\boldsymbol{C}} \boldsymbol{\gamma}_0 \tag{8}$$

can be set up. Hereby $\boldsymbol{C} \equiv (\boldsymbol{J}_{\boldsymbol{F}})^T \boldsymbol{J}_{\boldsymbol{F}}$ is the Right Cauchy-Green-Strain-

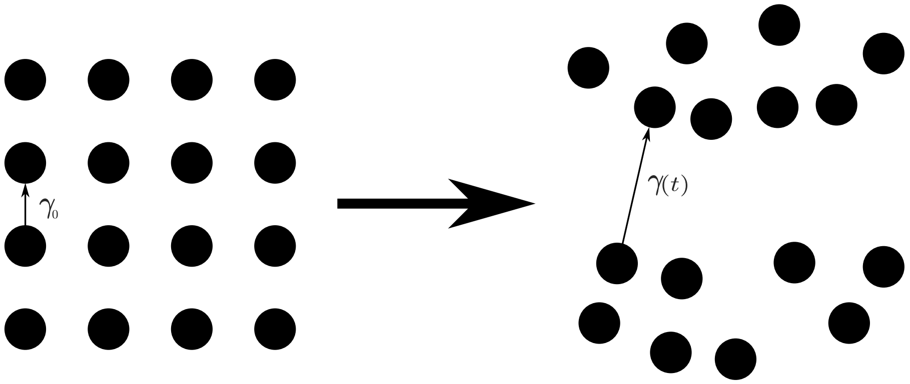

Fig. 3. Schematic positions of particles at the initial time t_0 (left) and at the later time t (right).

Tensor, in the following just named Cauchy-Green-Strain-Tensor (CGST) [22]. From the CGST, a quantitative value for the largest stretch at the observed position $\boldsymbol{x}_0$ is achieved by finding the eigenvector $\boldsymbol{\xi}_1$ corresponding to the largest eigenvalue $\sqrt{\lambda_1}$ of $\boldsymbol{R}$ and setting the vector $\boldsymbol{\gamma}_0$ equal to it, such that

$$\boldsymbol{\gamma}^T\boldsymbol{\gamma} = \lambda_1\boldsymbol{\gamma}_0^T\boldsymbol{\gamma}_0 \Rightarrow \sqrt{\frac{\boldsymbol{\gamma}^T\boldsymbol{\gamma}}{\boldsymbol{\gamma}_0^T\boldsymbol{\gamma}_0}} = \sqrt{\lambda_1} \tag{9}$$

holds. This is the largest deformation at the observed position after the integration time $\Delta t := t_\mathrm{F} - t_0$. With the largest eigenvalue λ_1 of the CGST the Forward FTLE (FFTLE)

$$\Lambda^+(\boldsymbol{x}_0, t_0, \Delta t) := \frac{1}{\Delta t}\cdot\ln\sqrt{\lambda_1\left(\boldsymbol{F}_{t_0}^{t_0+\Delta t}(\boldsymbol{x}_0)\right)} \tag{10}$$

can be calculated [59]. In the same way the whole calculation can be conducted backwards in time such that an initial set of particles is observed and the configuration which led to this ensemble is retrieved. For this purpose another time interval $[t_0 - \Delta t,\, t_0] \subset \mathscr{T}$ is observed and the flow map $\boldsymbol{F}_{t_0}^{t_0-\Delta t}(\boldsymbol{x}_0)$ has to be taken into account. The result is the Backward FTLE (BFTLE)

$$\Lambda^-(\boldsymbol{x}_0, t_0, \Delta t) := \frac{1}{\Delta t}\cdot\ln\sqrt{\lambda_1\left(\boldsymbol{F}_{t_0}^{t_0-\Delta t}(\boldsymbol{x}_0)\right)}. \tag{11}$$

The FTLE is a function of the initial position $\boldsymbol{x}_0$, the initial time t_0 and the considered time interval. For a given time interval, repelling Lagrangian Coherent Structures (rLCS) can be defined as those material lines (in 2D) or material surfaces (in 3D) that are simply connected local maxima of the FFTLE according to Eq. (10) [38,60]. These isosurfaces, also called FTLE-ridges, are surfaces which can be interpreted as "barriers" which hinder transport of species across it during the observed time interval. In the same way, attracting Lagrangian Coherent Structures (aLCS) can be defined as the material lines or surfaces which are simply connected local maxima of the BFTLE according to Eq. (11). If in contrast the zones of highest mixing during this time interval are of interest, the Finite Time Lyapunov Mixing Intensity (FTLMI) $\widetilde{\Lambda} := \sqrt{\Lambda^+\cdot\Lambda^-}$ can be calculated [36]. Where this value is high, both is true: Particles have come from far away and will separate quickly and thus, a high mixing efficiency results. A low value on the other hand indicates either strong attraction or strong repulsion, but not both. Finally, a very low value indicates zones where both effects play a minor role and almost no mixing takes place during the observed time interval.

For a more mathematical and strict definition of the LCSs, a closer look on the eigenvalues $0 < \lambda_3 \le \lambda_2 \le \lambda_1$ and corresponding eigenvectors $\boldsymbol{\xi}_1, \boldsymbol{\xi}_2, \boldsymbol{\xi}_3$ is necessary. Farazmand and Haller [23] derived four criteria which have to be fulfilled unconditionally by a material line or surface to be an LCS. While this procedure is implemented in LCS-Tool [24] for 2D flows, this work deals with 3D flows. The analysis concerning the necessary criteria for existence remains challenging for 3D flows. Therefore, LCSs will be approximated as ridges in the FTLE-fields [61].

2.2.2. Trajectory-based network methods for identification of coherent sets

Let $\boldsymbol{x}_i(t) \in \Omega,\ i = 1, \ldots, N_\mathrm{P}$ be particle trajectories according to Eq. (2), which are evaluated at discrete times $t_l \in \mathscr{T},\ l = 1, \ldots, N_\mathrm{T}$. For setting up a trajectory-network the approach proposed by Schneide et al. [50] is followed. A threshold $\varepsilon > 0$ is fixed and at each time step instantaneous adjacency matrices $\boldsymbol{A}_l \in \{0,1\}^{N_\mathrm{P}}$, with entries $a_{ij,l} = 1$ if $\|\boldsymbol{x}_i(t_l) - \boldsymbol{x}_j(t_l)\|_2 < \varepsilon$ for $i \neq j$ and $a_{ij,l} = 0$ otherwise, are built. MATLAB's `rangesearch` implements such an ε-neighborhood search. From the family of adjacency matrices $\boldsymbol{A}_l$ the network weight matrix

$$\boldsymbol{W} = \sum_{l=1}^{N_\mathrm{T}} \boldsymbol{A}_l \tag{12}$$

is obtained. This symmetric matrix stores the information on how often a particle j was in the direct ε-neighbourhood of another particle i. So the entry w_{ij} is large if the trajectories of tracers i and j are close for a long time. With the weight matrix the degree matrix $\boldsymbol{D}$ can be constructed, a diagonal matrix with entries

$$d_{ii} := \sum_{j=1}^{N_\mathrm{P}} w_{ij}, \tag{13}$$

where d_{ii} encodes how many contacts a specific particle i has had during the observed discrete time interval. This value will be high for particles in regions where a high mixing efficiency arises. A low value indicates regions of poor mixing efficiency. This can also be formally related to FTLE [62] and is similar in spirit to the trajectory encounter volume proposed in [63].

Coherent compartments that mitigate global mixing can be identified by spectral clustering. In particular, a normalised cut problem [64] is solved, with the N_P particles (or their trajectories) forming the vertices and the links represented in the weight matrix $\boldsymbol{W}$. To this end, the generalised eigenvalue problem [45]

$$\boldsymbol{L}\boldsymbol{v} = \lambda\boldsymbol{D}\boldsymbol{v}, \tag{14}$$

with non-negative eigenvalues $0 = \lambda_1 \le \lambda_2 \le \ldots \le \lambda_{N_\mathrm{P}}$ is considered. Hereby $\boldsymbol{L} := \boldsymbol{D} - \boldsymbol{W}$ is the non-normalised Laplacian. In particular, $\boldsymbol{v}_1 = (1 \ \cdots \ 1)^T$ is an eigenvector to the eigenvalue $\lambda_1 = 0$. According to Fiedler, such graph is connected if and only if the algebraic multiplicity of the eigenvalue λ_1 is 1, and hence $\lambda_2 > 0$ [65]. If $\lambda_2, \ldots, \lambda_k$ with $k < N_\mathrm{P}$ are close to zero and $\lambda_{k+1} \gg \lambda_k$, the network is decoupled into k communities that are only loosely connected [48,65]. The corresponding eigenvectors $\boldsymbol{v}_1, \ldots, \boldsymbol{v}_k \in \mathbb{R}^{N_\mathrm{P}}$ carry the spatial information about the different partitions. The basis $\boldsymbol{V} := (\boldsymbol{v}_1, \ldots, \boldsymbol{v}_k)$ of the eigenspace $\mathscr{V} \subset \mathbb{R}^{N_\mathrm{P}}$

can be transformed into a sparse basis $\boldsymbol{U} := (\boldsymbol{u}_1, \dots, \boldsymbol{u}_k)$ of the vector space $\mathscr{U}$, such that $\mathscr{U} \approx \mathscr{V}$ using the SEBA algorithm developed by Froyland et al. [66]. The entry in the m^{th} row of the n^{th} column of the matrix $\boldsymbol{U}$ delivers the likelihood of component m belonging to the cluster n. By choosing a threshold, each component m can be assigned to a specific coherent cluster n or to the incoherent background, respectively [50,66]. The vector $\boldsymbol{S}_{\max} \in \mathbb{R}^{N_{\mathrm{P}}}$, which describes an overall cluster likelihood for each particle with entries $s_m = \max_n u_{mn}$ can also be considered.

2.2.3. Lattice Boltzmann simulations

The fluid velocity $\boldsymbol{w}$ in this work is retrieved by using a simulation utilising the LBM, conducted with M-Star 3.6.13 (M-Star Simulations, LLC, Ellicott City, MD, USA). Since this work does not focus on the application of the LBM, this procedure will only be explained briefly here. A more detailed description of the LBM was presented by Hofmann et al. [52]. A complete in depth derivation of the whole method can be found in the books by Krüger et al. [67] or Succi [68].

To retrieve the macroscopic velocity field, the Boltzmann equation

$$\frac{\partial f}{\partial t} + \boldsymbol{\zeta}^T \nabla_x f + \boldsymbol{F}_{\mathrm{ext}}^T \nabla_\zeta f = K(f) \tag{15}$$

is solved numerically for a set of particles with the particle distribution function f. These particles are not equal to the particles mentioned in chapter 2.2.1, but represent molecular particles, moving in the observed geometry Ω, colliding and tending to achieve an equilibrium distribution. Hereby are $\boldsymbol{\zeta}$ the velocity of these particles, $\boldsymbol{F}_{\mathrm{ext}}$ the external forces and K the collision parameter. As collision parameter the Bhatnagar-Gross-Krook collision parameter

$$K(f) = -\frac{1}{t_{\mathrm{R}}} \cdot (f - f^{\mathrm{eq}}) \tag{16}$$

with the relaxation time t_{R} and the equilibrium particle distribution density f^{eq} is used [67]. For the modelling of turbulence, an LES is conducted utilising the Smagorinsky-Lilly subgrid-scale model [69] with a Smagorinsky constant of $C_{\mathrm{S}} = 0.1$ [51,70,71]. Macroscopic variables, hence density and momentum, can be retrieved from the numerical solution of the Boltzmann equation via [72]

$$\rho \equiv \int f(\boldsymbol{x}, \boldsymbol{\zeta}, t) d\boldsymbol{\zeta} \approx \sum_i f_i \tag{17}$$

$$\rho \boldsymbol{w} \equiv \int \boldsymbol{\zeta} f(\boldsymbol{x}, \boldsymbol{\zeta}, t) d\boldsymbol{\zeta} \approx \sum_i \boldsymbol{c}_i f_i. \tag{18}$$

All simulations were carried out on a cluster with two AMD Epyc 7702 64 core processors and two Nvidia Tesla A100 GPUs.

2.3. Computational setup

The whole procedure consists of several steps. The first one is to achieve the fluid velocity field by means of the LBM. Then, in MATLAB, perfectly flow-following particles are advected by the interpolated fluid velocity field to yield the positions after a time Δt. With the initial and the final particle positions, the FTLE is calculated using an in-house developed MATLAB code. The whole algorithm is depicted in Fig. 4. Each step will be presented one by one in the following.

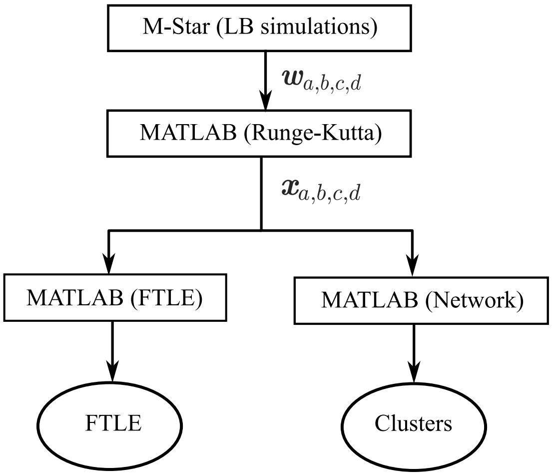

Fig. 4. Flow chart.

Retrieving the velocity field

The simulations are carried out using M-Star CFD 3.6.13. First, the geometry is loaded into the programme. The physical parameters of the fluid are chosen to match the values given in Section 2.1. Stirrer frequencies of $n \in \{252\,\mathrm{rpm}, 450\,\mathrm{rpm}\}$ are used, since for these stirrer frequencies experimental validation has been carried out [51,52]. An equidistant grid with 300 lattice points across the vessel's diameter is chosen. This yields a distance between lattice points of $\Delta x_{\mathrm{L}} = 0.42\,\mathrm{mm}$. This value was found to match the necessary condition of a grid independent simulation and additionally shows a sufficient resolution for the following calculation of particle trajectories. It also accounts for sufficiently high resolved turbulence effects. A Courant number of $Co = 0.05$ is used to guarantee stability. The calculated velocity data is saved every $\Delta t_{\mathrm{sim}} = 10^{-3}\,\mathrm{s}$, which yields the discrete fluid velocity field in space and time $\boldsymbol{w}_{a,b,c,d} \approx \boldsymbol{w}(x_a, y_b, z_c, t_d)$.

Interpolation and advection of particles

At each point of interest $\boldsymbol{x}_{a,b,c}$, a perfectly flow-following particle is positioned at the time t_0. The initial distance between neighbouring particles is Δx. The trajectories of these particles are calculated by solving the differential equation

$$\dot{\boldsymbol{x}}_{a,b,c} = \boldsymbol{w}\left(\boldsymbol{x}_{a,b,c}(t), t\right), \quad \boldsymbol{x}_{a,b,c}(t_0) = \boldsymbol{x}_{a,b,c,0} \tag{19}$$

on $[t_0, t_{\mathrm{F}}]$ using the solver `ode45`, which is implemented in MATLAB. The solver `ode45` utilises an embedded fifth order Runge-Kutta routine based on the Butcher tableau derived by Dormand and Prince [73]. The discrete fluid velocity field is interpolated linearly to achieve the velocities the positions in-between. For the purpose of the calculation of the FTLE-fields, only the first $\boldsymbol{x}_{a,b,c,0} := \boldsymbol{x}_{a,b,c}(t_0)$ and the final position $\boldsymbol{x}_{a,b,c,\mathrm{F}} := \boldsymbol{x}_{a,b,c}(t_{\mathrm{F}})$ over the time interval $[t_0, t_{\mathrm{F}}]$ are relevant and used for further analysis. The trajectory-based network requires the positions at additional points in time in this given interval are necessary.

Calculation of the FTLE

With the calculated positions, the Jacobian of the flow map can be calculated at each discrete point $\boldsymbol{x}_{a,b,c} \in \Omega$. Since there are only discrete values, the Jacobian has to be approximated by means of the central difference scheme

$$\boldsymbol{J_F} = \begin{pmatrix} \frac{\partial F_1}{\partial x} & \frac{\partial F_1}{\partial y} & \frac{\partial F_1}{\partial z} \\ \frac{\partial F_2}{\partial x} & \frac{\partial F_2}{\partial y} & \frac{\partial F_2}{\partial z} \\ \frac{\partial F_3}{\partial x} & \frac{\partial F_3}{\partial y} & \frac{\partial F_3}{\partial z} \end{pmatrix} \approx \begin{pmatrix} \frac{x_{a+1,b,c,\mathrm{F}} - x_{a-1,b,c,\mathrm{F}}}{x_{a+1,b,c,0} - x_{a-1,b,c,0}} & \frac{x_{a+1,b,c,\mathrm{F}} - x_{a-1,b,c,\mathrm{F}}}{y_{a+1,b,c,0} - y_{a-1,b,c,0}} & \frac{x_{a+1,b,c,\mathrm{F}} - x_{a-1,b,c,\mathrm{F}}}{z_{a+1,b,c,0} - z_{a-1,b,c,0}} \\ \frac{y_{a,b+1,c,\mathrm{F}} - y_{a,b-1,c,\mathrm{F}}}{x_{a,b+1,c,0} - x_{a,b-1,c,0}} & \frac{y_{a,b+1,c,\mathrm{F}} - y_{a,b-1,c,\mathrm{F}}}{y_{a,b+1,c,0} - y_{a,b-1,c,0}} & \frac{y_{a,b+1,c,\mathrm{F}} - y_{a,b-1,c,\mathrm{F}}}{z_{a,b+1,c,0} - z_{a,b-1,c,0}} \\ \frac{z_{a,b,c+1,\mathrm{F}} - z_{a,b,c-1,\mathrm{F}}}{x_{a,b,c+1,0} - x_{a,b,c-1,0}} & \frac{z_{a,b,c+1,\mathrm{F}} - z_{a,b,c-1,\mathrm{F}}}{y_{a,b,c+1,0} - y_{a,b,c-1,0}} & \frac{z_{a,b,c+1,\mathrm{F}} - z_{a,b,c-1,\mathrm{F}}}{z_{a,b,c+1,0} - z_{a,b,c-1,0}} \end{pmatrix}. \tag{20}$$

The FFTLE and BFTLE can now be achieved by calculating the largest eigenvalue of the approximated CGST by means of MATLAB's function `eig` and application of either Eq. (10) or (11), respectively.

3. Results and discussion

In the following, the results of the numerical simulations will be presented and discussed. The first part 3.1 focuses on the FTLE for different settings with an identification of possible compartments and mixing or dead zones. In the second part 3.2, the focus is on the necessity to use an instantaneous velocity field instead of a time-averaged one for the calculation of the FTLE and the mixing dynamics. In the third and final part 3.3, the findings are complemented by an examination of the trajectory-based network and the determined clusters. The schematic sketch of the observed plane for evaluation is depicted in Fig. 5.

3.1. *Mixing analysis with the Finite Time Lyapunov Exponent*

The long time evaluation of the FTLE was carried out by observing the FTLE-field arising from an integration of particles over a time equivalent to three stirrer revolutions. The results shown in Fig. 6 indicate that for the observed time interval, the highest values the Forward and the Backward FTLE-fields can be found around the stirrer, indicating both a strong mixing and possible ridges as bounds of compartments for both stirrer frequencies. Another important information which can be taken from these FTLE-fields is the very low values arising in the upper region of the vessel in positive z-direction. Even for this long integration time, almost no mixing occurred during three stirrer revolutions in this region as seen in Fig. 6. The reason for this is quite obvious. This position is on the opposite side of a baffle, yielding a weaker mixing performance than in the upper region on the baffle's side.

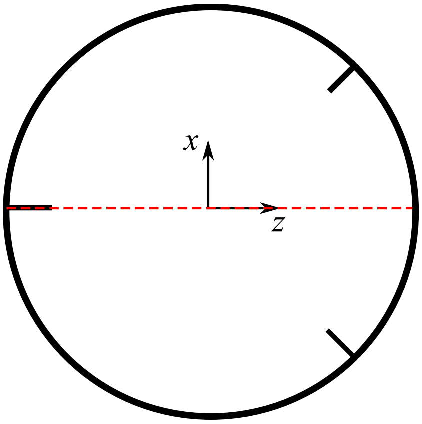

Fig. 5. Schematic sketch of the position of the evaluation plane (dashed line), top view.

On the slice $32.5\,\mathrm{mm} \leq z \leq 65\,\mathrm{mm}$, high BFTLE values are visible, denoting a large area of attraction. An effect of the higher stirrer frequency of $n = 450\,\mathrm{rpm}$ can be observed in the plots of both FTLE-fields. It is clearly shown that the magnitude of stretching and attraction is higher in the whole vessel, compared to the case with a stirrer frequency of $n = 252\,\mathrm{rpm}$. Additionally, there is a significant larger amount of small scale FTLE ridges between the two stirrers, due to the stronger turbulence. For a better identification of LCSs and compartments it is necessary to reduce the integration time Δt. In the following, only the findings for the stirrer frequency of $n = 252\,\mathrm{rpm}$ are shown, since they resemble those for $n = 450\,\mathrm{rpm}$. In Fig. 7, the FFTLE and BFTLE are shown for an integration time corresponding to $2/3$ stirrer revolutions. Defining an a/rLCS as a ridge in the B/FFTLE-field, the results suggest an appearance of both kinds in the stirrer planes, while the lower one is oriented slightly diagonally, turning towards the vessel's bottom. The BFTLE additionally indicates a high amount of small scale aLCS candidates at various positions, especially between the two stirrers, as already seen in the longtime evaluation. The earlier mentioned zone of poor mixing in the upper part of the reactor is also visible here. Due to the scaling of the colour bar it does not look as impactful during this short time interval. A closer look on the values though shows a higher ratio between the FTLE values around the stirrer and the FTLE values in the zone of poor mixing compared to the ratio for the long time FTLE-field. An investigation of the upper stirrer plane reveals that the values towards the centre of the reactor are high, the values at the outer regions are quite small and no persistent ridge from the centre to the wall is visible. For a further analysis, the FFTLE and BFTLE in the y-normal direction at the upper stirrer height of $y = 0.12\,\mathrm{m}$ are depicted in Fig. 8. As can be seen, the ridge appears only in the centre of the reactor for the FFTLE and as ring around the stirrer for the BFTLE. This leads to the assumption that mixing in this area will be high but no compartmentalisation will arise at this height due to the low repulsion near the vessel's wall.

Up to this point, the FTLE-fields were only examined for different integration times with a defined, fixed initial starting point in time t_0. The following analysis focuses on the influence of this starting time t_0. For this purpose, the geometric mean of the FFTLE was calculated for a shifting starting time $t_{0,k} = 60\,\mathrm{s} + k{\cdot}0.01\,\mathrm{s}$, where $k = 0, \ldots, 72$ with a fixed integration time Δt during three stirrer revolutions. After the calculation of the FTLE-fields, the geometric mean

$$\widehat{\Lambda}^{+}(\boldsymbol{x}_0, \Delta t) := \sqrt[73]{\Pi_{k=0}^{72} \Lambda^{+}(\boldsymbol{x}_0, 60\,\mathrm{s} + k{\cdot}0.01\,\mathrm{s}, \Delta t)} \tag{21}$$

was calculated. This is depicted together with the standard deviation from this geometric mean in Fig. 9. The result reinforces the earlier statements. Also here, high FTLE values can be seen around the stirrers with the same orientation. Even the zone of low interaction at $z > 0$, $y > 200\,\mathrm{mm}$ can be identified in the mean FTLE-field for this integration time. The standard deviation on the other hand shows a

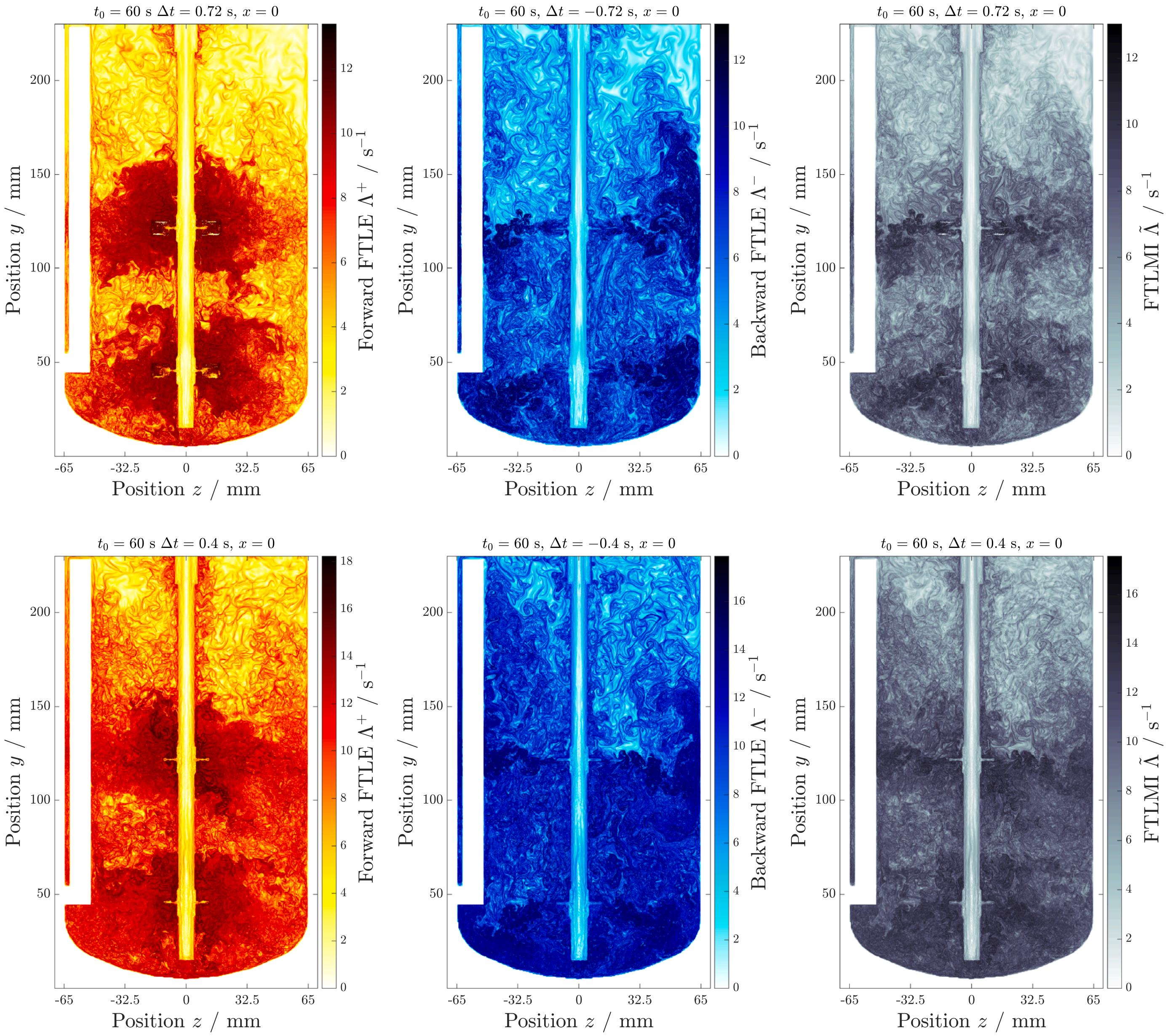

Fig. 6. FFTLE (left), BFTLE (middle) and FTLMI (right) with an initial resolution of $\Delta x = 100$ μm and an integration time equivalent to three stirrer revolutions. Top: $n = 252$ rpm, bottom: $n = 450$ rpm.

behaviour which has not been expected immediately. The highest variance can be found around the region of high FTLE values as an envelope. This leads to the assumption that the highest interaction, hence the highest mixing intensity can also be found here. Furthermore, it shows that the overall locations of the FTLE-ridges vary only little during the course of stirring. This will be further investigated, conducting the trajectory-based network methods and the identification of clusters or compartments, but first a closer look on the necessity to use a time-dependent fluid velocity field will be taken.

3.2. The influence of a time-averaged fluid velocity field

The FTLE-fields for the time-averaged case were retrieved by the calculation of the flow map according to Eq. (2) but using a time-averaged fluid velocity field $\overline{\boldsymbol{w}}(\boldsymbol{x})$. This resulting mean fluid velocity field is a function of only the position $\boldsymbol{x}$ but not of time t, hence the trajectories of the particles match the streamlines of the mean flow. The time-averaging was done by taking the average of the velocity during the time interval [30 s, 60 s]. The results are depicted in Fig. 10. It can be seen clearly that there is a huge difference to the time dependent case discussed in Section 3.1, Fig. 6. While the highest FTLE values are in the same order of magnitude but slightly lower, the FTLE ridges themselves look very differently. The local, relatively high FTLE values, which can be observed by taking the time-dependent velocity fields, are completely filtered out in the time-averaged case. Nevertheless, the position of the global maxima of both the FFTLE and BFTLE can be found again at the same heights. Indeed these positions appear as a sharp line, allowing to localise them better than in the time dependent simulations. But while the FTLE-ridge did not reach from the centre to the wall in the time-dependent case, in the time-averaged one it does. This is a huge difference since this finding implies a sharp compartmentalisation in the dynamics of the mean velocity field that is non-existent in the real, time-dependent case. Due to this reason, an identification of LCSs according to the definition as ridges in the FTLE-field and compartments could be possible by neglecting the transient effects, but the results are an over-prediction. Also, for a detailed study of all transient effects that a fluid

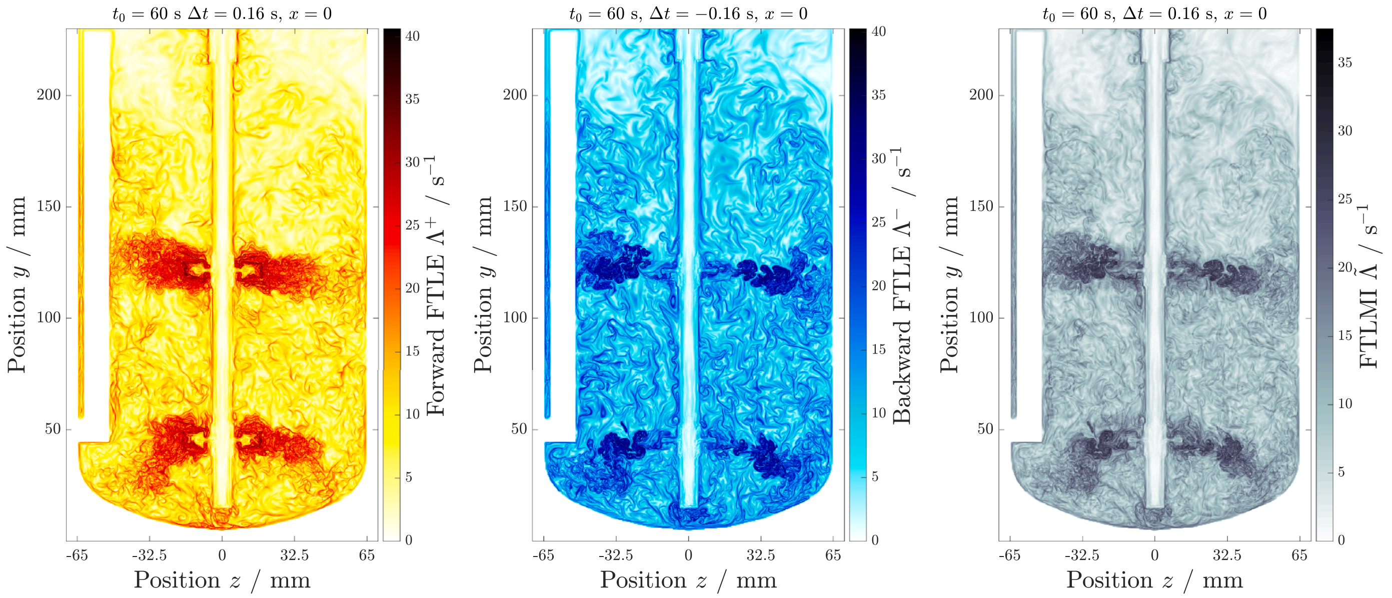

Fig. 7. FFTLE (left), BFTLE (middle) and FTLMI (right) with an initial resolution of $\Delta x = 100$ μm and an integration time equivalent to 2/3 stirrer revolutions for a stirrer frequency of $n = 252$ rpm.

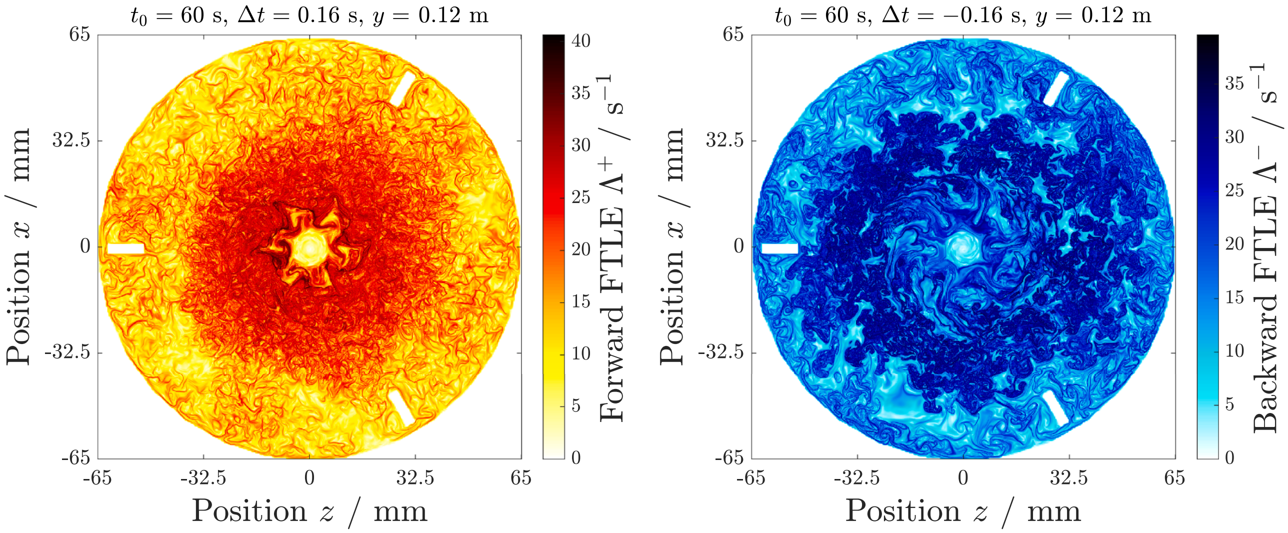

Fig. 8. FFTLE (left) and BFTLE (right) at the upper stirrer plane with an initial resolution of $\Delta x = 100$ μm and an integration time equivalent to 2 /3 stirrer revolutions for a stirrer frequency of $n = 252$ rpm.

parcel experiences, it is significant to take these time-dependent effects into account.

Nevertheless, time-averaging seems to be a fair choice to identify the general positions of ridges in the FTLE-field when hard drive disk space has to be saved or only mean velocity fields are available from experiments. The transient fluid velocity data for a stirrer frequency of 252 rpm takes about 250 GB hard drive disc space for the non-averaged case compared to 1.4 GB for the averaged case. Nevertheless, many effects are suppressed doing so. If the user is interested in the behaviour of the apparatus in regions where the FTLE does not reach its global maximum or the overall mixing behaviour, they are advised to consider the time-dependent velocity field. Additionally, time-averaging is only possible in meaningful manner if the flow shows some degree of periodicity, as it is most often the case for STRs. If this is not the case, time-averaging of the velocity field to calculate the FTLE will deliver results which do not allow any significant interpretation at all. The most important issue with the Lagrangian analysis with a time-averaged fluid velocity field is that it delivers boundaries of compartments which did not appear using a transient fluid velocity field.

3.3. Trajectory-based network and compartments

The trajectory-based network analysis was conducted with MATLAB. In total 342,208 particle trajectories, initialised on a regular three-dimensional grid with mesh size 2 mm at time $t_0 = 60$ s are considered. As output the particle positions in time increments of 10 ms, on $[t_0, t_0 + \Delta t]$, where $\Delta t = 720$ ms are taken, resulting in $N_\mathrm{T} = 73$ discrete time steps. For $\varepsilon = 3$ mm, the instantaneous adjacency matrices to set up the network weight matrix $\boldsymbol{W}$ and the corresponding degree matrix $\boldsymbol{D}$ are built. The 20 smallest eigenvalues of the generalised graph Laplacian eigenvalue problem are computed by means of MATLAB's function `eigs`. While the first eigenvector $\boldsymbol{v}_1$ to the single eigenvalue $\lambda_1 = 0$ is constant, eigenvectors $\boldsymbol{v}_2, \ldots, \boldsymbol{v}_5$ contain information about coherent compartments as shown in Fig. 11. Note that for better comparison with

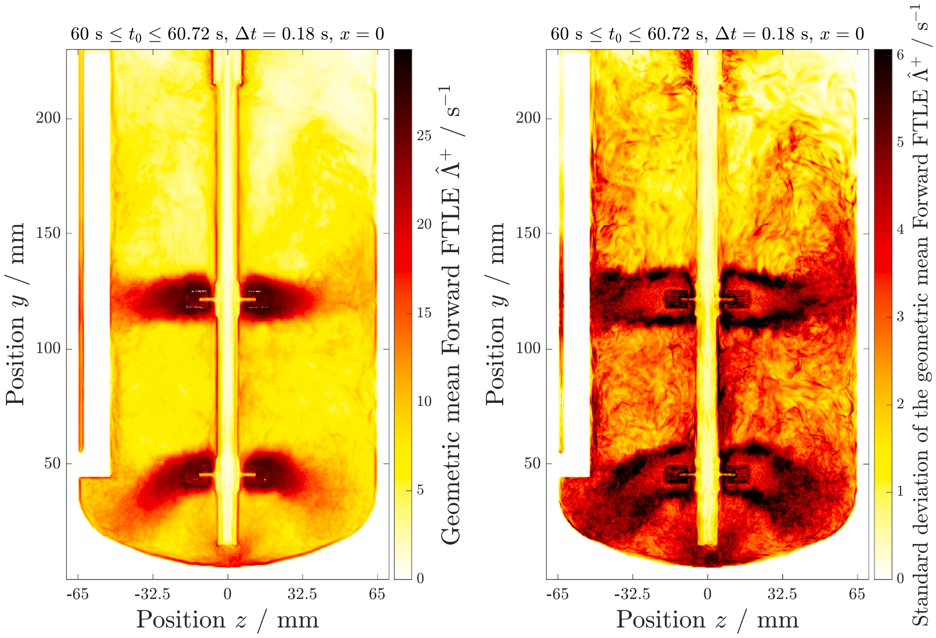

Fig. 9. Geometric mean (left) of the FFTLE and its standard deviation (right) for a sliding time interval with an initial resolution of Δx = 100 μm for a stirrer frequency of n = 252 rpm.

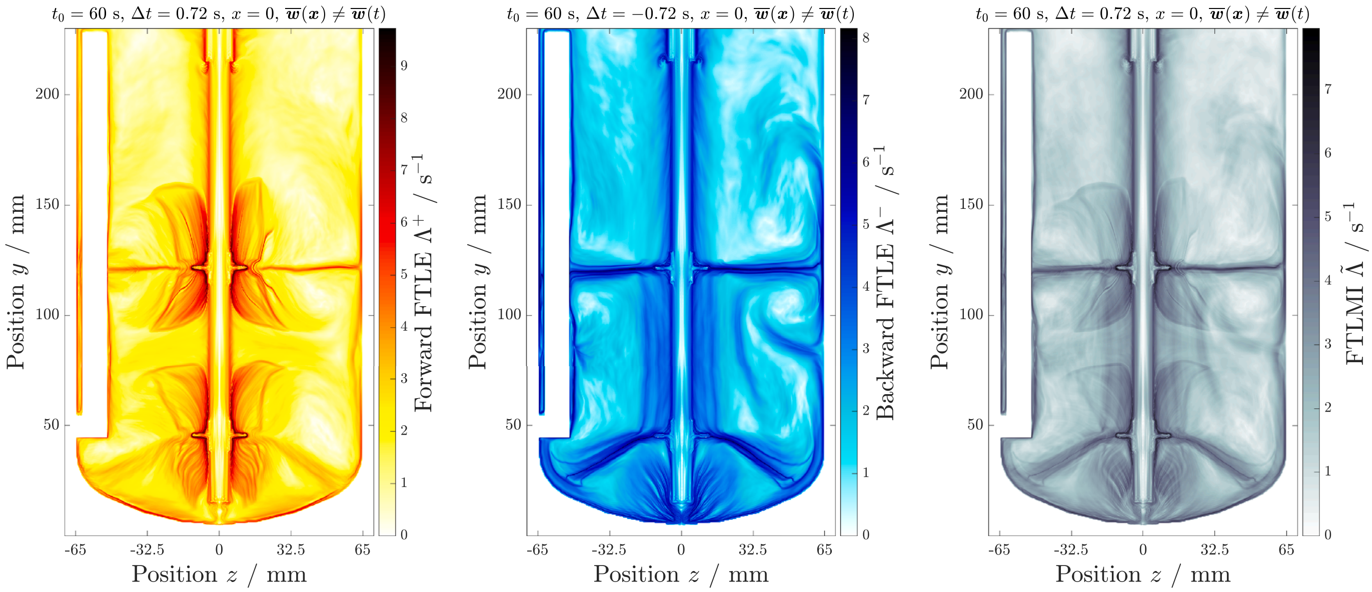

Fig. 10. FFTLE (left), BFTLE (middle) and FTLMI (right) with an initial resolution of Δx = 100 μm and an integration time corresponding to three stirrer revolutions with a time-averaged velocity field for a stirrer frequency of n = 252 rpm.

the FTLE results, the eigenvector data, which is available for the whole three-dimensional vessel, is plotted restricted to the $x = 0$ plane, i.e. the 6,335 initial conditions on that plane are coloured according to the respective eigenvector entries. In particular, v_2 highlights regions at the top and the bottom of the vessel, whereas v_3 and v_4 (not shown) provide finer partitions of the top region. v_5 highlights a central region.

To identify coherent compartments from these leading eigenvectors, the sparse eigenbasis approximation approach SEBA [66] is employed and a cluster indicator $S_{\max}$ is obtained. The result from such a post-processing of v_1, v_2 is shown in Fig. 12 (left), where again the three-dimensional results are restricted to the $x = 0$ plane. Here a coherent region at the bottom of the vessel is identified and one at the top, indicated by high $S_{\max}$ values. Five coherent sets are obtained, when $v_1, \ldots, v_5$ are considered, see Fig. 12 (right). In this plot only four of them are visible due to the orientation of the plane. In particular, a coherent compartment in the centre of the vessel is identified. Interestingly, the two coherent sets at the bottom and the centre of the vessel are characterised by strong internal mixing as also the FTLE studies show. Note that the high FTLE values occur right in the middle of the two lower compartments and do not coincide with the boundaries of these compartments as could naively be expected. The three top compartments appear to be dead zones with very limited dynamics. The coherent sets with respect to the whole three-dimensional vessel can then be extracted by means of setting a threshold to the cluster indicator. In Fig. 13, only those particles are shown at initial (left) and final time (right) for which the $S_{\max}$ cluster indicator exceeds 0.75.

Altogether, the findings achieved by the trajectory-based network indicate five compartments: one around the lower stirrer, one around

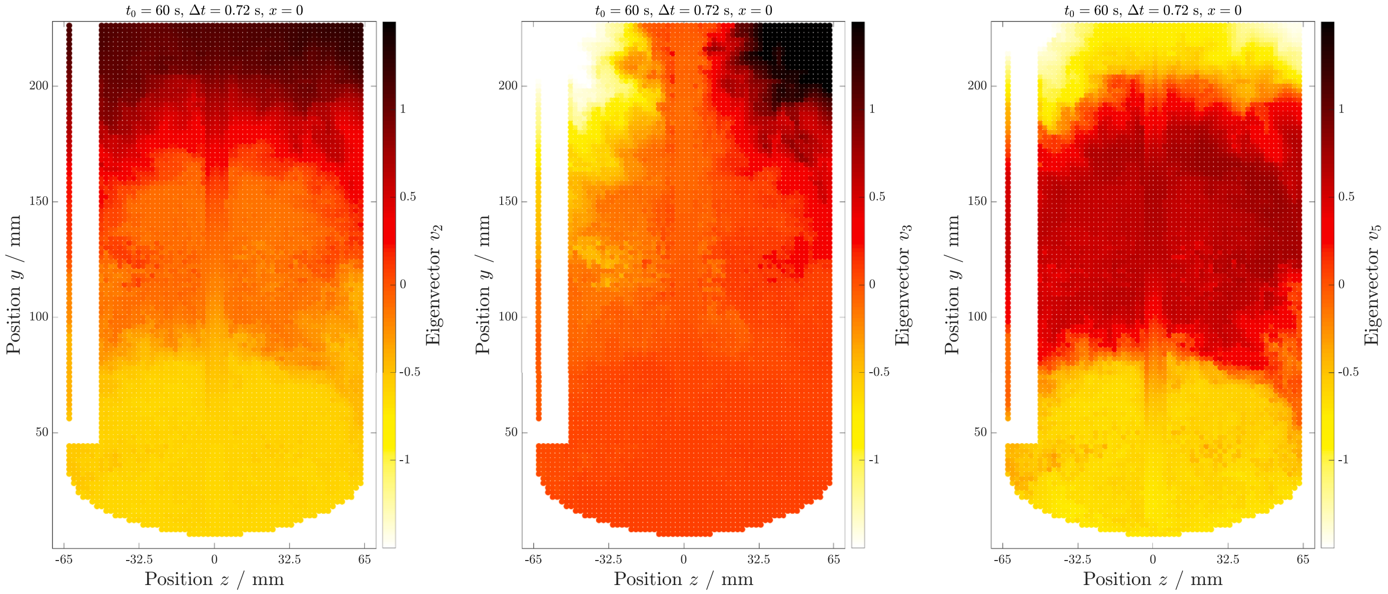

Fig. 11. Leading eigenvectors of the graph Laplacian eigenvalue problem highlight coherent sets.

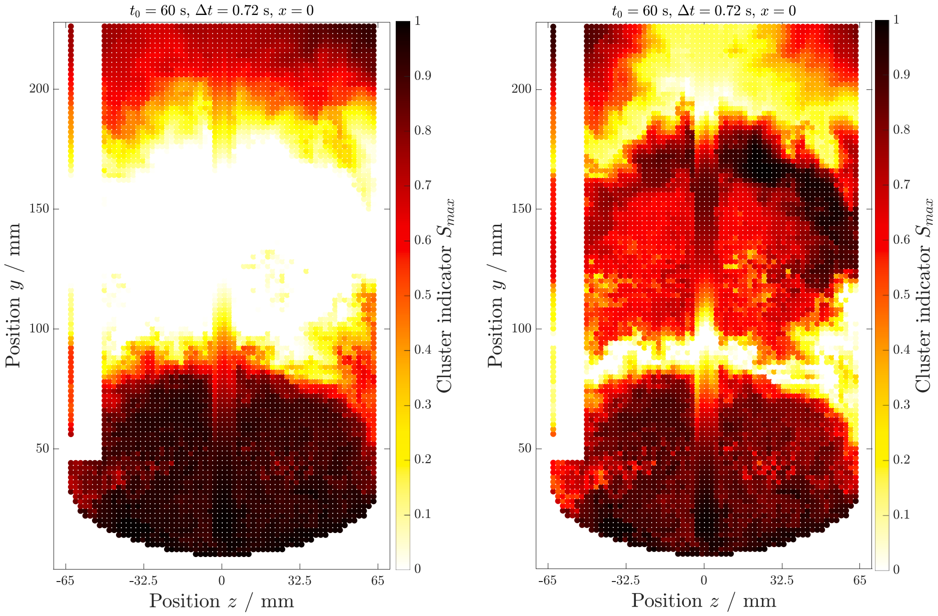

Fig. 12. Identification of coherent sets via the sparse eigenbasis approximation SEBA. Left: two coherent sets, located at the top and the bottom of the reactor, are obtained from the first two eigenvectors. Right: SEBA applied to the first five eigenvectors gives a more refined picture of the mixing compartments.

the upper stirrer and three between the respective baffles in the upper region of the vessel. The transport between compartments seems to be very low, while the interaction of particles belonging to the same compartment is quite high. These transient compartments evolve in the course of the process.

4. Conclusion

In this work, the flow in a laboratory-scale STR was analysed by Lagrangian methods. The required fluid velocity field was simulated by means of the LBM using the commercial programme M-Star CFD 3.6.13. With the fluid velocity field, Lagrangian analyses according to both the FTLE and trajectory-based network methods were conducted. To retrieve the FTLE-field, an in-house developed MATLAB code based on the LCS Tool [24] was used. The code is not restricted to data generated by M-Star CFD alone, but can also be applied to any kind of CFD or experimental data after some minor adjustments. Hence, the whole calculation conducted in this work can be executed with the same programme for every kind of data set. The trajectory-based network was calculated following the approach of Padberg-Gehle and Schneide [48]. The calculation of one transient fluid velocity field took about six hours, the calculation of one FTLE-field on the x-normal plane took about 20 minutes. The time needed for the calculation and evaluation of the trajectory-based network was less than two hours.

As main result of this work, transient compartments, their positions and the internal dynamics were identified. The trajectory-based network analysis yielded five separated clusters or transient compartments, positioned around the bottom level stirrer, directly around the top level stirrer and between the baffles in the upper region of the reactor respectively. The analysis of the three-dimensional FTLE-field delivers a

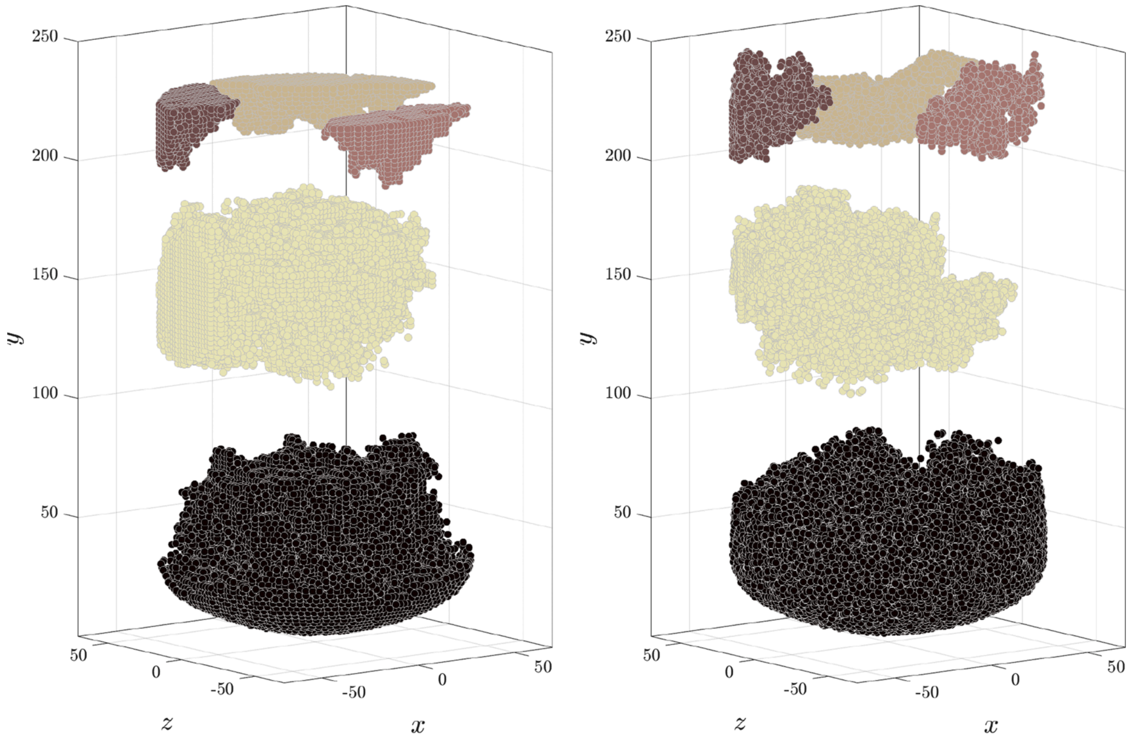

Fig. 13. Extraction of five coherent sets: only those particles are shown for which the $S_{\max}$ cluster indicator exceeds 0.75. Left: particle positions at $t_0 = 60$ s; right: particle positions at $t_0 + \Delta t = 60.72$ s. While there appears to be strong mixing within the detected compartments, there is no transport between them in the considered time span of $\Delta t = 720$ ms.

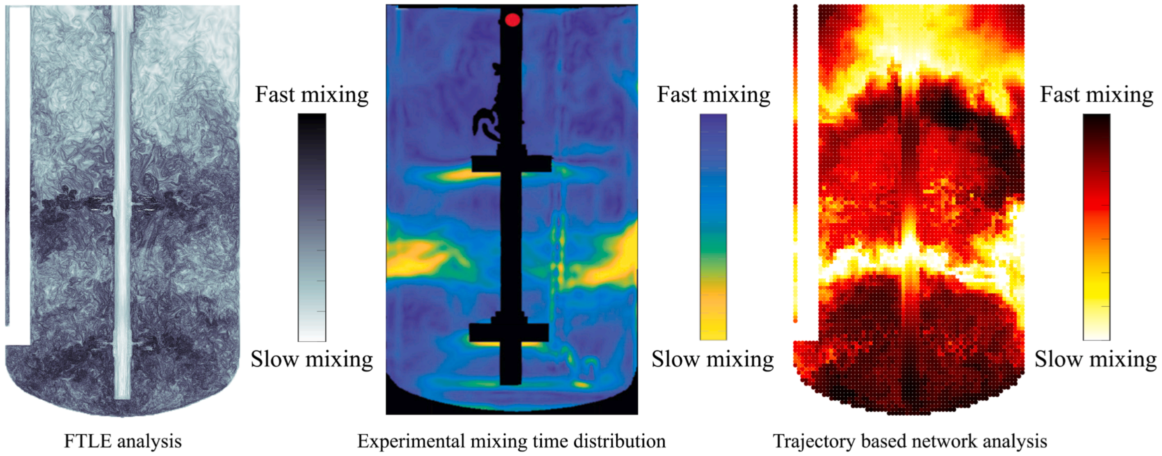

Fig. 14. Qualitative comparison between the Lagrangian results of this work and experimental data from Fitschen [10], the red dot marks the feed position during the respective experiment.

different result. The ridges in these fields can be found directly at the stirrers for both the time-averaged and the transient case. While the time-averaged fluid velocity field implies a sharp separation, a closer look on the resulting FTLE-field using a transient fluid velocity field shows that a compartmentalisation in this area is unlikely to happen since the ridge does not cover the vessel's whole cross section at the stirrer's height. Furthermore, both analyses concerning the mixing efficiency, depicted by the FTLMI $\widetilde{\Lambda}$ and the cluster indicator $S_{\max}$, compare Figs. 6 and 12, deliver the same areas of high interaction and thus high mixing efficiency. This is only true for the transient case and cannot be reproduced for the FTLMI calculated from the mean velocity field.

In Fig. 14, a qualitative comparison between the Lagrangian data of this work and experimental results [10] concerning the absolute local mixing time distribution is given. The experimental results match the findings from the trajectory-based network analysis and the transient FTLMI analysis qualitatively, yielding the same positions of compartment boundaries and regions of high interaction, even if the stirrers are slightly shifted in the experimental setup, about 18 mm above those used in this work.

In summary, the combination of the used Lagrangian analysis tools, the examination of the three-dimensional FTLE-field and the trajectory-based network approach, delivers invaluable insight into the mixing processes taking place in an STR. With this knowledge it is possible to improve various processes such as fermentations efficiently by adjusting e.g. the positions of feed inlets. Additionally, the findings of this work show, that using a time-averaged fluid velocity field delivers distorted results which do not mirror the real processes taking place, and that the observation of FTLE-ridges alone is not sufficient to detect LCSs or boundaries of compartments.

Data and Code Availability

Please contact the corresponding authors to obtain access to the data.

Declaration of Competing Interest

The authors declare that they have no conflict of interest.

Data availability

Data will be made available on request.

Acknowledgements

The authors gratefully acknowledge the financial support provided by the German Research Foundation (DFG) within the project 395843083 (KA 4854/1-1) and the project 316204571 as part of the Priority Programme DFG-SPP 1881 “Turbulent Superstructures”.

The authors thank Johannes Wutz from M-Star Simulations, LCC. for the fruitful discussions.

Further, the authors thank Marc Maly and Sebastian Hofmann for proofreading.

References

[1] M. Zlokarnik. Stirring: Theory and Practice, Wiley-VCH, Weinheim ; New York, 2001.

[2] S.I.A. Shah, L.W. Kostiuk, S.M. Kresta, et al., The effects of mixing, reaction rates, and stoichiometry on yield for mixing sensitive reactions-part I: model development, Int. J. Chem. Eng. 2012 (2012) 1–16, https://doi.org/10.1155/2012/750162.URL http://www.hindawi.com/journals/ijce/2012/750162/

[3] L. Rudniak, P.M. Machniewski, A. Milewska, E. Molga, et al., CFD modelling of stirred tank chemical reactors: homogeneous and heterogeneous reaction systems, Chem. Eng. Sci. 59 (22-23) (2004) 5233–5239, https://doi.org/10.1016/j.ces.2004.09.014.URL https://linkinghub.elsevier.com/retrieve/pii/S0009250904006694

[4] L. Gaugler, Y. Mast, J. Fitschen, S. Hofmann, M. Schlüter, R. Takors, Scaling-down biopharmaceutical production processes via a single multi-compartment bioreactor (SMCB), Eng. Life Sci. (2022), https://doi.org/10.1002/elsc.202100161. elsc.202100161

[5] E.H. Stitt, Alternative multiphase reactors for fine chemicals A world beyond stirred tanks? Chem. Eng. J. (2002) 14.

[6] J. Fitschen, S. Hofmann, J. Wutz, A.v. Kameke, M. Hoffmann, T. Wucherpfennig, M. Schlüter, et al., Novel evaluation method to determine the local mixing time distribution in stirred tank reactors, Chem. Eng. Sci.: X 10 (2021) 100098, https://doi.org/10.1016/j.cesx.2021.100098.URL https://linkinghub.elsevier.com/retrieve/pii/S2590140021000113

[7] A. Rosseburg, J. Fitschen, J. Wutz, T. Wucherpfennig, M. Schlüter, et al., Hydrodynamic inhomogeneities in large scale stirred tanks - influence on mixing time, Chem. Eng. Sci. 188 (2018) 208–220, https://doi.org/10.1016/j.ces.2018.05.008.URL https://linkinghub.elsevier.com/retrieve/pii/S0009250918302999

[8] Y.-X. Dai, Z.-H. Wang, Y.-W. Fan, Z.-Q. Cheng, et al., Analysis of mixing effect and power consumption of cone-bottom dual Rushton turbines stirred tank, Chem. Pap. 76 (4) (2022) 2177–2191, https://doi.org/10.1007/s11696-021-02010-1.

[9] Q. Kang, J. Liu, X. Feng, C. Yang, J. Wang, et al., Isolated mixing regions and mixing enhancement in a high-viscosity laminar stirred tank, Chin. J. Chem. Eng. 41 (2022) 176–192, https://doi.org/10.1016/j.cjche.2021.11.008.URL https://linkinghub.elsevier.com/retrieve/pii/S1004954121005760

[10] J. Fitschen. Hydrodynamic Characterization of Heterogeneities in Aerated Stirred Tank Reactors: From an Eulerian to a Lagrangian Perspective, 1. auflage, Cuvillier Verlag, Göttingen, 2022.Doctoral Dissertation, Hamburg University of Technology

[11] F. Maluta, A. Paglianti, G. Montante, et al., Towards a CFD-PBE simulation of aerated stirred tanks at high gas hold ups and different flow regimes, Chem. Eng. Res. Des. 180 (2022) 425–436, https://doi.org/10.1016/j.cherd.2021.10.018.URL https://linkinghub.elsevier.com/retrieve/pii/S0263876221004287

[12] F. Maluta, F. Alberini, G. Montante, A. Paglianti, et al., Validation of a procedure for the numerical simulations of gas-liquid stirred tanks by means of a computational fluid dynamics approach, Can. J. Chem. Eng. 100 (12) (2022) 3472–3485, https://doi.org/10.1002/cjce.24548.

[13] C. Haringa, An analysis of organism lifelines in an industrial bioreactor using Lattice-Boltzmann CFD, Eng. Life Sci. (2022), https://doi.org/10.1002/elsc.202100159.elsc.202100159

[14] C. Haringa, W. Tang, A.T. Deshmukh, J. Xia, M. Reuss, J.J. Heijnen, R.F. Mudde, H. J. Noorman, et al., Euler-Lagrange computational fluid dynamics for (bio)reactor scale down: an analysis of organism lifelines, Eng. Life Sci. 16 (7) (2016) 652–663, https://doi.org/10.1002/elsc.201600061.

[15] P. Eibl, S. Rustige, C. Witz, J. Khinast, et al., LBM for two-phase (bio-)reactors. Advances in Chemical Engineering 55, Elsevier, 2020, pp. 219–285, https://doi.org/10.1016/bs.ache.2020.04.003.

[16] J. Fitschen, M. Maly, A. Rosseburg, J. Wutz, T. Wucherpfennig, M. Schlüter, et al., Influence of spacing of multiple impellers on power input in an industrial-scale aerated stirred tank reactor, Chem. Ing. Tech. 91 (12) (2019) 1794–1801, https://doi.org/10.1002/cite.201900121.

[17] M. Xie, J. Xia, Z. Zhou, J. Chu, Y. Zhuang, S. Zhang, et al., Flow pattern, mixing, gas hold-up and mass transfer coefficient of triple-impeller configurations in stirred tank bioreactors, Ind. Eng. Chem. Res. 53 (14) (2014) 5941–5953, https://doi.org/10.1021/ie400831s.

[18] P. Vrábel, R.G.J.M. Van der Lans, Y.Q. Cui, K.C.A.M. Luyben, Compartment model approach: mixing in large scale aerated reactors with multiple impellers, Chem. Eng. Res. Des. 77 (4) (1999) 291–302, https://doi.org/10.1205/026387699526223.URL https://www.sciencedirect.com/science/article/pii/S0263876299717892

[19] Y.-Q. Cui, R. van der Lans, H. Noorman, K.C.A.M. Luyben, Compartment mixing model for stirred reactors with multiple impellers, Chem. Eng. Res. Des. 74 (1996) 261–271.

[20] G. Haller, G. Yuan, Lagrangian coherent structures and mixing in two-dimensional turbulence, Phys. D: Nonlinear Phenom. 147 (3-4) (2000) 352–370, https://doi.org/10.1016/S0167-2789(00)00142-1.URL https://linkinghub.elsevier.com/retrieve/pii/S0167278900001421

[21] T. Peacock, G. Haller, Lagrangian coherent structures: the hidden skeleton of fluid flows, Phys. Today 66 (2) (2013) 41–47, https://doi.org/10.1063/PT.3.1886.

[22] G. Haller, Lagrangian Coherent Structures, Annual Review of Fluid Mechanics 47 (2015) 137–162.

[23] M. Farazmand, G. Haller, Computing Lagrangian coherent structures from their variational theory, Chaos: Interdiscip. J. Nonlinear Sci. 22 (1) (2012) 013128, https://doi.org/10.1063/1.3690153.

[24] K. Onu, F. Huhn, G. Haller, et al., LCS tool : a computational platform for Lagrangian coherent structures, J. Comput. Sci. 7 (2015) 26–36, https://doi.org/10.1016/j.jocs.2014.12.002.ArXiv:1406.3527 [nlin]

[25] F. Lekien, S.C. Shadden, J.E. Marsden, et al., Lagrangian coherent structures in n-dimensional systems, J. Math. Phys. 48 (6) (2007) 065404, https://doi.org/10.1063/1.2740025.

[26] S.C. Shadden, C.A. Taylor, Characterization of coherent structures in the cardiovascular system, Ann. Biomed. Eng. 36 (7) (2008) 1152–1162, https://doi.org/10.1007/s10439-008-9502-3.

[27] S.C. Shadden, M. Astorino, J.-F. Gerbeau, et al., Computational analysis of an aortic valve jet with Lagrangian coherent structures, Chaos: Interdiscip. J. Nonlinear Sci. 20 (1) (2010) 017512, https://doi.org/10.1063/1.3272780.

[28] S.C. Shadden, Lagrangian coherent structures, in: R. Grigoriev (Ed.). Transport and Mixing in Laminar Flows, Wiley-VCH Verlag GmbH & Co. KGaA, Weinheim, Germany, 2011, pp. 59–89, https://doi.org/10.1002/9783527639748.ch3.

[29] S. Balasuriya, Explicit invariant manifolds and specialised trajectories in a class of unsteady flows, Phys. Fluids 24 (12) (2012) 127101, https://doi.org/10.1063/1.4769979.

[30] S. Balasuriya, R. Kalampattel, N.T. Ouellette, et al., Hyperbolic neighbourhoods as organizers of finite-time exponential stretching, J. Fluid Mech. 807 (2016) 509–545, https://doi.org/10.1017/jfm.2016.633.URL https://www.cambridge.org/core/product/identifier/S0022112016006339/type/journal_article

[31] S. Balasuriya, N.T. Ouellette, I.I. Rypina, et al., Generalized Lagrangian coherent structures, Phys. D: Nonlinear Phenom. 372 (2018) 31–51, https://doi.org/10.1016/j.physd.2018.01.011.URL https://linkinghub.elsevier.com/retrieve/pii/S0167278917302750

[32] S.L. Brunton, C.W. Rowley, Fast computation of finite-time Lyapunov exponent fields for unsteady flows, Chaos: Interdiscip. J. Nonlinear Sci. 20 (1) (2010) 017503, https://doi.org/10.1063/1.3270044.

[33] M. Sudharsan, S.L. Brunton, J.J. Riley, et al., Lagrangian coherent structures and inertial particle dynamics, Phys. Rev. E 93 (3) (2016) 033108, https://doi.org/10.1103/PhysRevE.93.033108.ArXiv:1512.05733 [physics]

[34] S.L. Brunton, C.W. Rowley, D.R. Williams, et al., Reduced-order unsteady aerodynamic models at low Reynolds numbers, J. Fluid Mech. 724 (2013) 203–233, https://doi.org/10.1017/jfm.2013.163.URL https://www.cambridge.org/core/product/identifier/S0022112013001638/type/journal_article

[35] C.G. Llamas, C. Spille, S. Kastens, D.G. Paz, M. Schlüter, A. Kameke, et al., Potential of Lagrangian analysis methods in the study of chemical reactors, Chem. Ing. Tech. 92 (5) (2020) 540–553, https://doi.org/10.1002/cite.201900147.

[36] A. von Kameke, S. Kastens, S. Rüttinger, S. Herres-Pawlis, M. Schlüter, et al., How coherent structures dominate the residence time in a bubble wake: an experimental example, 2019, ArXiv:1901.07081 [physics].

[37] K. Li, C. Savari, M. Barigou, et al., Computation of Lagrangian coherent structures from experimental fluid trajectory measurements in a mechanically agitated vessel, Chem. Eng. Sci. 254 (2022) 117598, https://doi.org/10.1016/j.ces.2022.117598. URL https://linkinghub.elsevier.com/retrieve/pii/S0009250922001828

[38] G. Haller, Distinguished material surfaces and coherent structures in three-dimensional fluid flows, Phys. D: Nonlinear Phenom. 149 (4) (2001) 248–277, https://doi.org/10.1016/S0167-2789(00)00199-8.

[39] G. Haller, An objective definition of a vortex, J. Fluid Mech. 525 (2005) 1–26, https://doi.org/10.1017/S0022112004002526.

[40] M.A. Green, C.W. Rowley, G. Haller, et al., Detection of Lagrangian coherent structures in three-dimensional turbulence, J. Fluid Mech. 572 (2007) 111–120, https://doi.org/10.1017/S0022112006003648.URL https://www.cambridge.org/core/product/identifier/S0022112006003648/type/journal_article

[41] M.R. Allshouse, T. Peacock, Lagrangian based methods for coherent structure detection, Chaos 25 (9) (2015) 097617, https://doi.org/10.1063/1.4922968.

[42] A. Hadjighasem, M. Farazmand, D. Blazevski, G. Froyland, G. Haller, A critical comparison of Lagrangian methods for coherent structure detection, Chaos 27 (5) (2017) 053104, https://doi.org/10.1063/1.4982720.

[43] G. Froyland, K. Padberg-Gehle, Almost-invariant and finite-time Coherent sets: directionality, duration, and diffusion, in: W. Bahsoun, C. Bose, G. Froyland (Eds.), Ergodic Theory, Open Dynamics, and Coherent Structures volume 70, Springer New York, New York, NY, 2014, pp. 171–216, https://doi.org/10.1007/978-1-4939-0419-8_9.Series Title: Springer Proceedings in Mathematics & Statistics

[44] G. Froyland, K. Padberg-Gehle, A rough-and-ready cluster-based approach for extracting finite-time coherent sets from sparse and incomplete trajectory data, Chaos 25 (8) (2015) 087406, https://doi.org/10.1063/1.4926372.

[45] A. Hadjighasem, D. Karrasch, H. Teramoto, G. Haller, et al., A spectral clustering approach to Lagrangian vortex detection, Phys. Rev. E 93 (6) (2016) 063107, https://doi.org/10.1103/PhysRevE.93.063107.ArXiv:1506.02258 [nlin]

[46] K.L. Schlueter-Kuck, J.O. Dabiri, Coherent structure colouring: identification of coherent structures from sparse data using graph theory, J. Fluid Mech. 811 (2017) 468–486.

[47] R. Banisch, P. Koltai, Understanding the geometry of transport: diffusion maps for Lagrangian trajectory data unravel coherent sets, Chaos 27 (3) (2017) 035804.

[48] K. Padberg-Gehle, C. Schneide, Network-based study of Lagrangian transport and mixing, Nonlinear Process. Geophys. 24 (4) (2017) 661–671, https://doi.org/10.5194/npg-24-661-2017.

[49] G. Iacobello, L. Ridolfi, S. Scarsoglio, A review on turbulent and vortical flow analyses via complex networks, Phys. A 563 (2021) 125476, https://doi.org/10.1016/j.physa.2020.125476.URL https://www.sciencedirect.com/science/article/pii/S0378437120307822

[50] C. Schneide, P.P. Vieweg, J. Schumacher, K. Padberg-Gehle, et al., Evolutionary clustering of Lagrangian trajectories in turbulent Rayleigh-Bénard convection flows, Chaos: Interdiscip. J. Nonlinear Sci. 32 (1) (2022) 013123, https://doi.org/10.1063/5.0076035.

[51] M. Kuschel, J. Fitschen, M. Hoffmann, A. von Kameke, M. Schlüter, T. Wucherpfennig, et al., Validation of novel lattice Boltzmann large Eddy simulations (LB LES) for equipment characterization in biopharma, Processes 9 (6) (2021) 950, https://doi.org/10.3390/pr9060950.

[52] S. Hofmann, C. Weiland, J. Fitschen, A. von Kameke, M. Hoffmann, M. Schlüter, Lagrangian sensors in a stirred tank reactor: comparing trajectories from 4d-particle tracking velocimetry and lattice-Boltzmann simulations, Chem. Eng. J. (2022) 137549, https://doi.org/10.1016/j.cej.2022.137549.

[53] M. Kraume (Ed.). Mischen und Rühren: Grundlagen und moderne Verfahren, Wiley-VCH, Weinheim, 2003.

[54] V.I. Arnold. Ordinary Differential Equations, MIT Press, [Cambridge, 1973.

[55] J. de la Villéon, F. Bertrand, P.A. Tanguy, R. Labrie, J. Bousquet, D. Lebouvier, et al., Numerical investigation of mixing efficiency of helical ribbons, AIChE J. 44 (4) (1998) 972–977, https://doi.org/10.1002/aic.690440423.

[56] J.M. Ottino. The Kinematics of Mixing: Stretching, Chaos, and Transport, Number 3 in Cambridge Texts in Applied Mathematics, Cambridge University Press, Cambridge ; New York, 1989.

[57] M.E. Gurtin. An Introduction TC Continuum Mechanics, Number No. v. 158 Mathematics in Science and Engineering, Academic Press, New York, 1981.

[58] V.I. Arnold, V.I. Arnold. Mathematical Methods of Classical Mechanics No. 60 in Graduate Texts in Mathematics, 2. ed., [7. korr. nachdr.], Springer, New York, 2001.

[59] G. Haller, T. Sapsis, Lagrangian coherent structures and the smallest finite-time Lyapunov exponent, Chaos: Interdiscip. J. Nonlinear Sci. 21 (2) (2011) 023115, https://doi.org/10.1063/1.3579597.

[60] G. Haller, Lagrangian coherent structures from approximate velocity data, Phys. Fluids 14 (6) (2002) 1851–1861, https://doi.org/10.1063/1.1477449.

[61] S.C. Shadden, F. Lekien, J.E. Marsden, et al., Definition and properties of Lagrangian coherent structures from finite-time Lyapunov exponents in two-dimensional aperiodic flows, Phys. D: Nonlinear Phenom. 212 (3-4) (2005) 271–304, https://doi.org/10.1016/j.physd.2005.10.007.URL https://linkinghub.elsevier.com/retrieve/pii/S0167278905004446

[62] R. Banisch, P. Koltai, K. Padberg-Gehle, et al., Network measures of mixing, Chaos: Interdiscip. J. Nonlinear Sci. 29 (6) (2019) 063125, https://doi.org/10.1063/1.5087632.

[63] I.I. Rypina, L.J. Pratt, et al., Trajectory encounter volume as a diagnostic of mixing potential in fluid flows, Nonlinear Process. Geophys. 24 (2) (2017) 189–202, https://doi.org/10.5194/npg-24-189-2017.

[64] J. Shi, J. Malik, Normalized Cuts and Image Segmentation, IEEE Trans. Pattern Anal. Mach. Intell. 22 (8) (2000) 18.

[65] M. Fiedler, Algebraic connectivity of graphs, Czechoslov. Math. J. 23 (2) (1973) 298–305, https://doi.org/10.21136/CMJ.1973.101168.

[66] G. Froyland, C.P. Rock, K. Sakellariou, et al., Sparse eigenbasis approximation: multiple feature extraction across spatiotemporal scales with application to coherent set identification, Commun. Nonlinear Sci. Numer. Simul. 77 (2019) 81–107, https://doi.org/10.1016/j.cnsns.2019.04.012.ArXiv:1812.02787 [math]

[67] T. Krüger, H. Kusumaatmaja, A. Kuzmin, O. Shardt, G. Silva, E.M. Viggen. The Lattice Boltzmann Method: Principles and Practice, Springer Berlin Heidelberg, New York, NY, 2016.

[68] S. Succi. The Lattice Boltzmann Equation: For Fluid Dynamics and Beyond Numerical Mathematics and Scientific Computation, Clarendon Press, 2001.URL https://books.google.de/books?id=OC0Sj_xgnhAC

[69] J. Smagorinsky, General circulation experiments with the primitive equations: I. The basic experiment*, Mon. Weather Rev. 91 (3) (1963) 99–164, https://doi.org/10.1175/1520-0493(1963)091<0099:GCEWTP>2.3.CO;2.

[70] H. Yu, S.S. Girimaji, L.-S. Luo, et al., DNS and LES of decaying isotropic turbulence with and without frame rotation using lattice Boltzmann method, J. Comput. Phys. 209 (2) (2005) 599–616, https://doi.org/10.1016/j.jcp.2005.03.022.URL https://linkinghub.elsevier.com/retrieve/pii/S0021999105001907

[71] J.J. Derksen, Numerical simulation of solids suspension in a stirred tank, AIChE J. 49 (11) (2003) 2700–2714, https://doi.org/10.1002/aic.690491104.

[72] L. M-Star Simulations, M-Star CFD Documentation, (https://docs.mstarcfd.com/theory/theoryNew.html), Last access: 16.12.2021.

[73] J.R. Dormand, P.J. Prince, A family of embedded Runge-Kutta formulae, J. Comput. Appl. Math. 6 (1) (1980) 19–26, https://doi.org/10.1016/0771-050X(80)90013-3.